

# Dynamic Mapping of Along-Track Ocean Altimetry: Method and Performance from Observing System Simulation Experiments

CLEMENT UBELMANN

*Jet Propulsion Laboratory, Pasadena, California*

BRUCE CORNUELLE

*Scripps Institution of Oceanography, La Jolla, California*

LEE-LUENG FU

*Jet Propulsion Laboratory, Pasadena, California*

(Manuscript received 11 August 2015, in final form 20 January 2016)

## ABSTRACT

Simulated along-track ocean altimetry data were used to implement the use of a nonlinear dynamic propagator to perform three-dimensional (time and 2D space) interpolation of mesoscale sea surface height (SSH). The method is an inverse approach to processing altimetry data unevenly sampled in time and space into high-level gridded altimetry maps. The inverse approach, similar to the standard objective mapping, contains some correction terms to the innovation vectors to account for nonlinear dynamics. Another key improvement is to solve for the covariance functions through a Green's function approach. From the Observing System Simulation Experiments carried out to simulate a three-satellite constellation over the Gulf Stream region, the new method can significantly reduce mapping errors and improve the resolving capabilities compared to the standard linear objective analysis such as that used by the AVISO gridding.

## 1. Introduction

Merging along-track ocean altimetry data into continuous maps in time and space is a challenging exercise that is extremely useful for research and applications. In particular, it provides synoptic views of the geostrophic currents and ocean dynamic content, not directly given by the along-track data. The most common gridded altimetry reconstructions (e.g., AVISO maps, <http://www.aviso.altimetry.fr/duacs/>, Aviso, 2015) from the available constellation of satellites are based on linear state analysis (following Bretherton, et al. 1976) with predefined time and space covariance models (e.g., Le Traon et al. 1998).

The mesoscale sea surface height (SSH) captured by altimetry satellites is principally dominated by quasi-geostrophically balanced dynamics (outside of the equatorial zone) that evolve with typical time scales of a few weeks and spatial scales of a few hundreds of

kilometers. The linear mapping analyses, as they have been performed so far, capture a significant part of these mesoscale dynamics (e.g., Ducet et al. 2000). These dynamics are known to be dominated, in large part, by the first baroclinic mode (e.g., Wunsch, 1997). Although well captured by the linear mapping, the actual evolution of the first baroclinic mode, especially at short spatial scales, is strongly nonlinear, which may limit the performance of the mapping. In Ubelmann et al. 2015, we have shown that accounting for the simplest nonlinear representation of the first baroclinic mode SSH evolution allows for significantly reducing interpolation errors between two fields of SSH, through the so-called dynamic interpolation. The fields of SSH were transported forward and backward by a nonlinear propagator conserving the potential vorticity expressed in the first baroclinic mode framework. This direct forward/backward approach, easy to implement, demonstrated the concept of dynamic interpolation, but was not directly applicable to observations unevenly sampled in time and space. In this present study, we propose to implement the use of this nonlinear propagator in an inverse approach,

---

*Corresponding author address:* Clement Ubelmann, Jet Propulsion Laboratory, 4800 Oak Grove Dr., Pasadena, CA 91109.  
E-mail: clement.ubelmann@jpl.nasa.gov

similar to the standard mapping analysis, allowing to process realistic along-track observations (of any distribution, with noise).

In the first section, we will briefly review the standard linear mapping analysis as commonly used for ocean altimetry data. Based on the same approach but introducing a correction term to the innovations, accounting for predictable nonlinear evolutions, we will propose in [section 2](#) the implementation of a propagator in the analysis to perform dynamic mapping. The method will be finally tested with Observing System Simulation Experiments (OSSEs) in the Gulf Stream region, described and analyzed in [section 3](#) globally and as a function of scale.

## 2. The standard mapping methods for altimetry data

The mapping methods commonly used for merging multisatellite altimetry data are based on a three-dimensional (time and space) linear analysis, applied to sea level anomaly (SLA) observations with respect to a background state (mean dynamic topography) and predefined time and space covariance functions for the departure from the background state.

$$C(\delta r, \delta t) = \langle \text{SLA}^2 \rangle \left[ 1 + \frac{\delta r}{L} + \frac{1}{6} \left( \frac{\delta r}{L} \right)^2 - \frac{1}{6} \left( \frac{\delta r}{L} \right)^3 \right] e^{-(\delta r/L)} e^{-(\delta t/t_0)^2} \\ = \langle \text{SLA}^2 \rangle \times f(\delta r) \times g(\delta t), \quad (3)$$

where  $\langle \text{SLA}^2 \rangle$  is the variance of SLA. In space (and for  $\delta t = 0$ ), the Fourier transform of this covariance function gives a power spectrum with a  $-4$  slope for wavelength  $\ll L$  and flat for wavelength  $\gg L$ . Here  $L = 150$  km is a typical value corresponding to a power spectrum generally similar to what is observed from along-track data (with an eddy band at approximately 250 km). In time (and for  $\delta r = 0$ ), the equivalent frequency power spectrum is flat for  $t \gg t_0$ , with a sharp cutoff for  $t \ll t_0$ . The westward propagation of eddies can also be accounted for by coupling  $\delta t$  and  $\delta r$  in Eq. (3) in a translating space as performed today in Aviso maps (e.g., [AVISO 2015](#)). In the experiments carried out for this study in the Gulf Stream current, we did not find a significant impact of accounting for westward propagation, so we will not consider it. Finally, the  $\mathbf{R}$  matrix is chosen accordingly with the best knowledge of measurement error. This error contains instrument error generally dominant at wavelength  $< 80$  km and known to be uncorrelated, contributing to the diagonal terms of  $\mathbf{R}$ . Other measurement errors, mostly from imperfect geophysical

## General formulation

If  $\mathbf{x}$  is the true state to estimate (referenced to the background) defined on a regular grid in space and time, the observations  $\mathbf{y}_0$  can be expressed as follows:

$$\mathbf{y}_0 = \mathbf{H}\mathbf{x} + \boldsymbol{\epsilon}_i, \quad (1)$$

where  $\mathbf{H}$  is the observation operator and  $\boldsymbol{\epsilon}_i$  is the measurement error (instrument and geophysical errors).

If we note  $\mathbf{B}_{s,t}$  as the expected covariance matrix of  $\mathbf{x}$  and  $\mathbf{R}$  the covariance matrix of measurement error between all pairs of observations, the state estimate  $\mathbf{x}_a$  is given by

$$\mathbf{x}_a = \mathbf{B}_{s,t} \mathbf{H}^T (\mathbf{H} \mathbf{B}_{s,t} \mathbf{H}^T + \mathbf{R})^{-1} \mathbf{y}_0, \quad (2)$$

where  $\mathbf{y}_0$  is the observation vector of SLA and  $\mathbf{T}$  denotes matrix transpose. For mesoscale circulations, covariance matrices  $\mathbf{B}_{s,t} \mathbf{H}^T$  (between grid and observation space) and  $\mathbf{H} \mathbf{B}_{s,t} \mathbf{H}^T$  (in observation space) can be typically filled explicitly with the following  $C$  function, depending only on the distance  $\delta r$  and the time offset  $\delta t$  (e.g., [Arhan and Colin de Verdière 1985](#)):

corrections, may contribute to off-diagonal terms (of larger scales).

## 3. The dynamic mapping using a nonlinear propagator

### a. The state estimation problem

As described in [Ubelmann et al. \(2015\)](#), it is possible to use a very simple but nonlinear propagator to account for a predictable part in the time evolution of the SSH signal, and as a result reduce the errors of the state estimate between SSH fields given at different times. In this section, we propose defining the state estimate problem using the nonlinear propagator with an inverse approach similar to the standard mapping method summarized above. This new implementation will allow dynamic reconstructions from realistic along-track data unevenly sampled in time and space.

The nonlinear propagator applied to a state of SSH is the time integration of Eq. (4) where the potential vorticity  $\mathbf{q}$  and the current function  $\boldsymbol{\psi}$  are defined in Eqs. (5) and (6):

$$\frac{\partial \mathbf{q}}{\partial t} + J(\boldsymbol{\psi}, \mathbf{q}) = 0, \quad (4)$$

$$\mathbf{q} = \nabla^2 \boldsymbol{\psi} - \frac{1}{L_R^2} \boldsymbol{\psi}, \quad \text{and} \quad (5)$$

$$\boldsymbol{\psi} = \frac{g}{f} \text{SSH}. \quad (6)$$

This propagator  $\mathcal{M}$  provides a transformation of the SSH field in time; it can be integrated forward and backward. Here  $\mathcal{M}$  naturally tends to diminish with time as there is no energy input but some numerical diffusion. However, we found that predictability skills decrease at a faster rate. We therefore propose to apply attenuation factor  $e^{-[(t-\text{tref})/t_p]^2}$  to the propagator, where  $t$  is the time variable and  $t_p$  is the time of predictability (possibly varying with the wavelength).

The goal is to estimate the true state of SLA at a particular time (time of analysis, noted  $\text{tref}$  in the following),  $\mathbf{x}^{\text{tref}}$ , from an ensemble of observations in a time window centered around  $\text{tref}$ . The true state at any time  $t$  around  $\text{tref}$ , noted  $\mathbf{x}^t$ , can be decomposed into a predictable term explained by the propagator integrated from  $\text{tref}$  (either forward or backward) and a nonpredictable term  $\mathbf{x}_{\text{nr}}^t$  accounting for all other nonresolved dynamics:

$$\mathbf{x}^t = \mathcal{M}(\mathbf{x}^{\text{tref}}) + \mathbf{x}_{\text{nr}}^t, \quad (7)$$

where  $\mathcal{M}(\mathbf{x}^{\text{tref}})$  is the predictable term and  $\mathbf{x}_{\text{nr}}^t$  is the contribution (from  $\text{tref}$  to  $t$ ) of the nonresolved dynamics. For  $t = \text{tref}$  by definition,  $\mathcal{M} = \mathbf{I}$  and  $\mathbf{x}_{\text{nr}}^t = 0$ . Over the time window, the better  $\mathcal{M}$  performs, the smaller  $\mathbf{x}_{\text{nr}}^t$  is. If we use Eq. (7) in Eq. (1), we obtain

$$\mathbf{y}_0 = \mathbf{H}[\mathcal{M}(\mathbf{x}^{\text{tref}}) + \mathbf{x}_{\text{nr}}^t] + \boldsymbol{\epsilon}_i. \quad (8)$$

The inverse problem consists of estimating  $\mathbf{x}^{\text{tref}}$  from the ensemble of observations  $\mathbf{y}_0$ . However, the nonlinearity of the operator  $\mathcal{M}$  prevents direct application of a linear least squares analysis. To solve this problem, we suppose that we know a first guess of the state at the reference time,  $\mathbf{x}_g^{\text{tref}}$ , sufficiently close to the truth  $\mathbf{x}^{\text{tref}}$  so that the propagator response to the guess error ( $\mathbf{x}_g^{\text{tref}} - \mathbf{x}^{\text{tref}}$ ) is quasi linear:

$$\mathcal{M}(\mathbf{x}^{\text{tref}}) \approx \mathcal{M}(\mathbf{x}_g^{\text{tref}}) + \mathbf{M}[\mathbf{x}^{\text{tref}} - \mathbf{x}_g^{\text{tref}}], \quad (9)$$

where  $\mathbf{M}$  is the linearized propagator around the guess  $\mathbf{x}_g^{\text{tref}}$ . In practice,  $\mathbf{x}_g^{\text{tref}}$  will be first obtained by a linear mapping, and then iteratively updated with the dynamic mapping solution, as detailed in the next section. By using Eq. (9), Eq. (8) becomes:

$$\mathbf{y}_0 - \mathbf{H}[\mathcal{M}(\mathbf{x}_g^{\text{tref}}) - \mathbf{M}\mathbf{x}_g^{\text{tref}}] = \mathbf{H}\mathbf{M}\mathbf{x}^{\text{tref}} + \mathbf{H}\mathbf{x}_{\text{nr}}^t + \boldsymbol{\epsilon}_i. \quad (10)$$

From this expression with linear rhs operators and known lhs terms, we can apply the least squares analysis

to estimate  $\mathbf{x}^{\text{tref}}$ , similarly to what was done from Eq. (1) to Eq. (2):

$$\mathbf{x}_a^{\text{tref}} = \mathbf{B}_s \mathbf{M}^T \mathbf{H}^T (\mathbf{H} \mathbf{M} \mathbf{B}_s \mathbf{M}^T \mathbf{H}^T + \mathbf{C}_{\text{nr}} + \mathbf{R})^{-1} \times \{\mathbf{y}_0 - \mathbf{H}[\mathcal{M}(\mathbf{x}_g^{\text{tref}}) - \mathbf{M}\mathbf{x}_g^{\text{tref}}]\}, \quad (11)$$

where  $\mathbf{B}_s$  is the covariance matrix for  $\mathbf{x}^{\text{tref}}$ , in space only because  $\mathbf{x}^{\text{tref}}$  is for a given time. Term  $\mathbf{C}_{\text{nr}}$  is the covariance matrix for the nonresolved dynamics in observation space, whose parameterization will be given later, and  $\mathbf{R}$  is the observational error covariance matrix. Equation (11) defines the solution of the dynamic interpolation problem. We can verify that if the propagator  $\mathcal{M}$  is linear,  $\mathcal{M} = \mathbf{M}$ ; the innovation term is the same as in the standard mapping. Term  $\mathbf{B}\mathbf{M}^T\mathbf{H}^T$  is the covariance of the true signal between the grid and observation locations, and  $\mathbf{H}\mathbf{M}\mathbf{B}\mathbf{M}^T\mathbf{H}^T + \mathbf{C}_{\text{nr}}$  is the covariance of the true signal in observation space, accounting for the resolved dynamics  $\mathbf{H}\mathbf{M}\mathbf{B}\mathbf{M}^T\mathbf{H}^T$  plus the independent nonresolved dynamics ( $\mathbf{C}_{\text{nr}}$ ). Therefore, if  $\mathcal{M}$  is linear, the problem is equivalent to a standard linear mapping.

#### b. Resolution in a reduced space using Green's functions

In the general case where  $\mathbf{M}$  is the linearized propagator of  $\mathcal{M}$ , the operator  $\mathbf{H}\mathbf{M}$  (from the model grid at the time of analysis to observation space at all times) of size (nobs,ngrid) would be burdensome to compute and store. However, since the expected wavelengths that can be resolved by altimetry mapping are limited (typically higher than 150 km), it is not necessary to operate the linearized propagator on the full model grid. If we transform the model grid in a reduced Fourier space containing a finite range of wavelengths, it is possible to consider only the linear response of a finite number of modes through the Green function approach (e.g., Wunsch, 1996, Menemenlis et al. 2005). To do so, we define a 2D Fourier orthogonal basis on which  $\mathbf{x}^{\text{tref}}$  can be decomposed as follows:

$$\mathbf{x}^{\text{tref}} = \boldsymbol{\Gamma}\boldsymbol{\eta}^{\text{tref}}, \quad (12)$$

where  $\boldsymbol{\eta}^{\text{tref}}$  is a vector of parameters to estimate, representing the amplitudes of the normalized Fourier modes defining the solution  $\mathbf{x}^{\text{tref}}$  and  $\boldsymbol{\Gamma}$  is the linear transformation from the Fourier space to the grid space. If we substitute  $\mathbf{x}^{\text{tref}}$  with  $\boldsymbol{\Gamma}\boldsymbol{\eta}^{\text{tref}}$  and  $\mathbf{x}_g^{\text{tref}}$  with  $\boldsymbol{\Gamma}\boldsymbol{\eta}_g^{\text{tref}}$ , where  $\boldsymbol{\eta}_g^{\text{tref}}$  is the vector of parameters for the guess, and if we note  $\mathbf{G} = \mathbf{H}\mathbf{M}\boldsymbol{\Gamma}$ , Eq. (10) becomes

$$\mathbf{y}_0 - \mathbf{H}[\mathcal{M}(\mathbf{x}_g^{\text{tref}}) - \mathbf{G}\boldsymbol{\eta}_g^{\text{tref}}] = \mathbf{G}\boldsymbol{\eta}^{\text{tref}} + \mathbf{x}_{\text{nr}}^t + \boldsymbol{\epsilon}_i, \quad (13)$$

where  $\mathbf{G}$  is the Green function matrix, representing the linear response (around the guess) of the modes in the

observation space (i.e., at observation times and locations). Its computation will be detailed in the following section. From any guess  $\mathbf{x}_g^{\text{tref}}$  (and its corresponding  $\boldsymbol{\eta}_g^{\text{tref}}$  parameters) the lhs terms of Eq. (13) can be computed (through backward/forward nonlinear propagator integration) and the rhs terms are linear operators. Hence, the least squares analysis can be applied to estimate the parameters  $\boldsymbol{\eta}^{\text{tref}}$ , similarly to what was done from Eq. (1) to Eq. (2):

$$\boldsymbol{\eta}_a^{\text{tref}} = \mathbf{P}\mathbf{G}^T(\mathbf{G}\mathbf{P}\mathbf{G}^T + \mathbf{C}_{\text{nr}} + \mathbf{R})^{-1} \times [\mathbf{y}_0 - \mathbf{H}\mathcal{M}(\mathbf{x}_g^{\text{tref}}) + \mathbf{G}\boldsymbol{\eta}_g^{\text{tref}}], \quad (14)$$

where  $\mathbf{P}$  is the covariance matrix of the parameters  $\boldsymbol{\eta}^{\text{tref}}$ . Since the Fourier modes are orthogonal in space (by definition),  $\mathbf{P}$  is diagonal and the variance terms must be chosen accordingly with the expected power spectrum of SLA, given for example by the Fourier transform of the autocorrelation function in Eq. (3). The solution of this equation, expressed in a reduced space, can be expressed back in the grid space by applying  $\mathbf{x}_a^{\text{tref}} = \mathbf{\Gamma}\boldsymbol{\eta}_a^{\text{tref}}$ . The main task is the computation of  $\mathbf{G}$  and the definition of an appropriate parameterization for  $\mathbf{C}_{\text{nr}}$ , described in the following.

### c. Computation of $\mathbf{G}$ matrix

For a given column  $j$  of the  $\mathbf{G}$  matrix, note that  $\mathbf{G}_{:,j}$  is the linear response of the propagator to the single mode  $\boldsymbol{\Gamma}_{:,j}$ , in the observation space. To obtain the linear response of the propagator, we propagate the mode with amplitude  $\alpha$  and rescale it after the propagator integration. Therefore,  $\mathbf{G}_{:,j}$  has the following expression:

$$\mathbf{G}_{:,j} = \mathbf{H}\mathbf{M}\boldsymbol{\Gamma}_{:,j} = \mathbf{H} \left[ \frac{\mathcal{M}(\mathbf{x}_g^{\text{tref}} + \alpha\boldsymbol{\Gamma}_{:,j}) - \mathcal{M}(\mathbf{x}_g^{\text{tref}})}{\alpha} \right]. \quad (15)$$

The factor  $\alpha$  should be small enough so that the response to the perturbation  $\alpha\boldsymbol{\Gamma}_{:,j}$  is linear, but large enough to avoid the effect of numerical truncation errors along the integration. In practice, there is a wide range of possible  $\alpha$  (typically of the order of a millimeter in SSH) leading to the same matrix. As shown by Eq. (15), the computation of  $\mathbf{G}$  requires the backward/forward propagator integration (over the time window containing the observations around tref) of all the single modes. Practically the amount of computation can still be reasonable since the propagator integration is very efficient.

### d. Parameterization of $\mathbf{C}_{\text{nr}}$ matrix

As mentioned earlier, we impose the variance of the propagator to decrease with time away from tref, following  $e^{-[(t-\text{tref})/t_p]^2}$ , where  $t_p$  is the time of predictability,

reflecting the skills of the propagator. However, the total variance of the true signal is not expected to decrease, but to remain constant because of unrepresented balance between dissipation and energy inputs. The latter will be implicitly considered in the nonresolved dynamics through the  $\mathbf{C}_{\text{nr}}$  matrix. Let us consider two locations in the time–space domain,  $r_1, t_1$  and  $r_2, t_2$  and denote  $\delta r = r_2 - r_1$  and  $\delta t = t_2 - t_1$ . Here  $t_1$  and  $t_2$  are defined from the reference time of analysis. If we assume that the total signal follows the covariance of Eq. (2),  $\langle \text{SLA}^2 \rangle \times f(\delta r) \times g(\delta t)$ , and that the propagator signal follows the same model with the exponential decay, and finally that  $\mathcal{M}(\mathbf{x}^{\text{tref}})$  and  $\mathbf{x}_{\text{nr}}^t$  are independent, we have  $\langle \text{SLA}^2 \rangle \times f(\delta r) \times g(\delta t) = \langle \text{SLA}^2 \rangle \times f(\delta r) \times e^{-(t_1^2/t_p^2)} e^{-(t_2^2/t_p^2)} + C_{\text{nr}}$ , where the  $C_{\text{nr}}$  function is the covariance of the nonresolved dynamics between the two locations. If we use the function  $g$  given in Eq. (3), the covariance model  $C_{\text{nr}}$  is the following:

$$C_{\text{nr}} = \langle \text{SLA}^2 \rangle \times f(\delta r) [e^{-(\delta t/t_0)^2} - e^{-[(t_1^2+t_2^2)/t_p^2]}]. \quad (16)$$

This covariance function  $C_{\text{nr}}$  will be used to fill the  $\mathbf{C}_{\text{nr}}$  matrix, expressed in the observation space.

## 4. The OSSEs

### a. Experiment setup

The outputs of an ocean general circulation model (OGCM) are used in the following as a reference truth from which an observation system is simulated, providing synthetic altimetric observations along virtual satellite tracks. The mapping methods presented above will be tested using these synthetic observations and the analyzed states will then be compared with the truth for performance estimation.

The OGCM fields come from a global MITgcm simulation at  $1/16^\circ$  horizontal resolution (Hill et al. 2007; Menemenlis et al. 2008) provided by the ECCO project. The Gulf Stream region has been chosen for this study, as shown in Fig. 1. The 6-hourly output fields over 1 year have been sampled by three virtual satellites, flying on Joint Altimetry Satellite Oceanography Network (Jason) orbits for the first two (shifted in time and space) and on Ka-band Altimeter (ALtiKa) orbit for the third one. The ground tracks are shown in Fig. 1. An instrument noise error has been added consistently with standard values of 3.3 cm at 1 Hz ( $\sim 5.5$ -km ground spacing) (Xu and Fu 2011)

The reference mean state (a mean dynamic topography from which covariance matrices will be defined) is the time-mean SSH of the simulation outputs. The observations  $\mathbf{y}_0$  are defined by the anomaly with the mean state plus the randomly generated instrument noise.

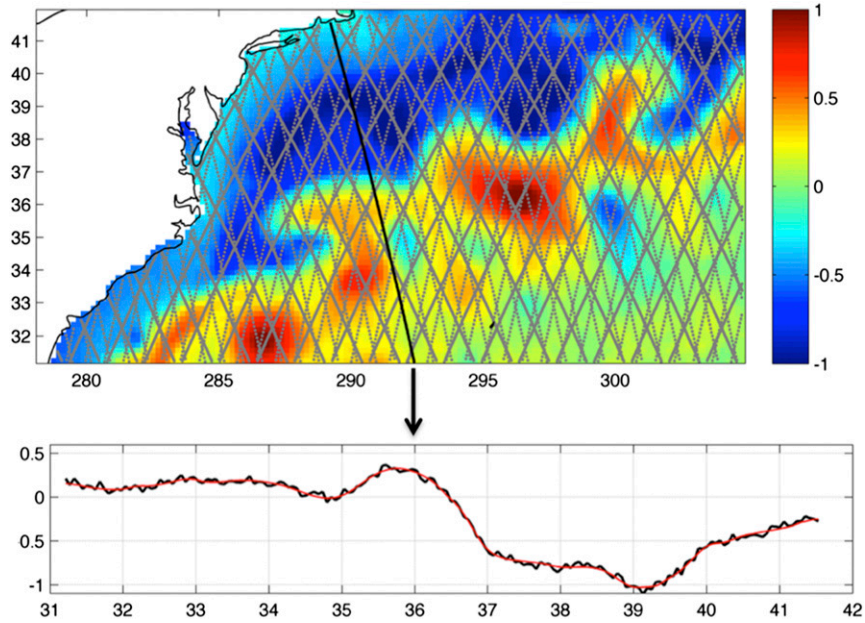


FIG. 1. (top) Snapshot of the reference SSH over the domain of interest and ground tracks of the constellation of satellite considered in the OSSEs. (bottom). Sampled SSH along a track (red) and synthetic observations (black) constituted of the sampled signal plus the random-generated instrument noise.

### b. Implementation of the mapping algorithms

The standard mapping solution has been first computed following the description in section 1. The following parameters have been chosen for the covariance model Eq. (3):  $t_0 = 15$  days,  $L = 150$  km, and  $\langle \text{SLA}^2 \rangle = 0.04 \text{ m}^2$ . Some tests with values ranging from 5 to 30 days and from 50 to 250 km for  $L$  were revealed to be above optimal values, which happen to be close to those currently found in the literature (e.g., Le Traon et al. 1998). This could be optimized by considering regional and seasonal dependences in further studies. To avoid large matrix inversions, the analysis is performed locally in time and space:  $\pm 20$  day time windows and a 400-km radius are chosen, knowing that correlation vanishes beyond a few hundreds of kilometers and beyond 20 days. In space, the local domains overlap every 100 km in zonal and meridional directions. Once computed, the local 2D solutions are linearly interpolated between the central locations of analysis. Finally, the matrix  $\mathbf{R}$  is chosen as diagonal, consistent with the level of instrumental error.

The dynamic mapping solution has then been computed following the description in section 2. The reduced Fourier basis  $\mathbf{\Gamma}$  is a 2D decomposition with wavelengths ranging from 100 to 800 km, where 800 km is the diameter of the local zone on which a single analysis is performed. The time windows are also  $\pm 20$  days. With this range of wavelength, the 2D Fourier

decomposition is composed of 192 modes, with each wavenumber containing two modes: a sine and a cosine. The diagonal of the  $\mathbf{Q}$  matrix is filled with the expected power spectral densities given by the Fourier transform of the autocorrelation function Eq. (3). The  $\mathbf{R}$  matrix is kept identical to the standard mapping case. The first guess used to compute the  $\mathbf{G}$  matrix is the solution from the standard mapping. As described in section 2, the computation of a single  $\mathbf{G}$  column is performed through the forward/backward propagator integration of the guess plus a small mode amplitude, minus the integration of the guess, and finally renormalized. An example of how a single mode evolves through that integration of the guess is shown in Fig. 2: a single column of the  $\mathbf{G}$  matrix is the integrated field (as represented in the bottom-right panel) located at observation points in time and space. The exponential decay of the propagator has been optimally set to  $t_p = 14$  days. With this value, the  $\mathbf{C}_{nr}$  matrix is filled following Eq. (16). Then, the solution  $\boldsymbol{\eta}_a^{\text{tréf}}$  can be computed by inverting  $(\mathbf{G}\mathbf{G}^T + \mathbf{C}_{nr} + \mathbf{R})$  and computing the product Eq. (14). The solution in the grid space is finally given by  $\mathbf{x}_a^{\text{tréf}} = \mathbf{\Gamma}\boldsymbol{\eta}_a^{\text{tréf}}$ . Since  $\mathbf{x}_a^{\text{tréf}}$  is closer to the truth than  $\mathbf{x}_g^{\text{tréf}}$  from the standard mapping solution, it is worth iterating a few times by updating the guess  $\mathbf{x}_g^{\text{tréf}}$  with the solution  $\mathbf{x}_a^{\text{tréf}}$ , so that the linearity hypothesis Eq. (9) is better verified. Convergence is typically obtained after three or four iterations.

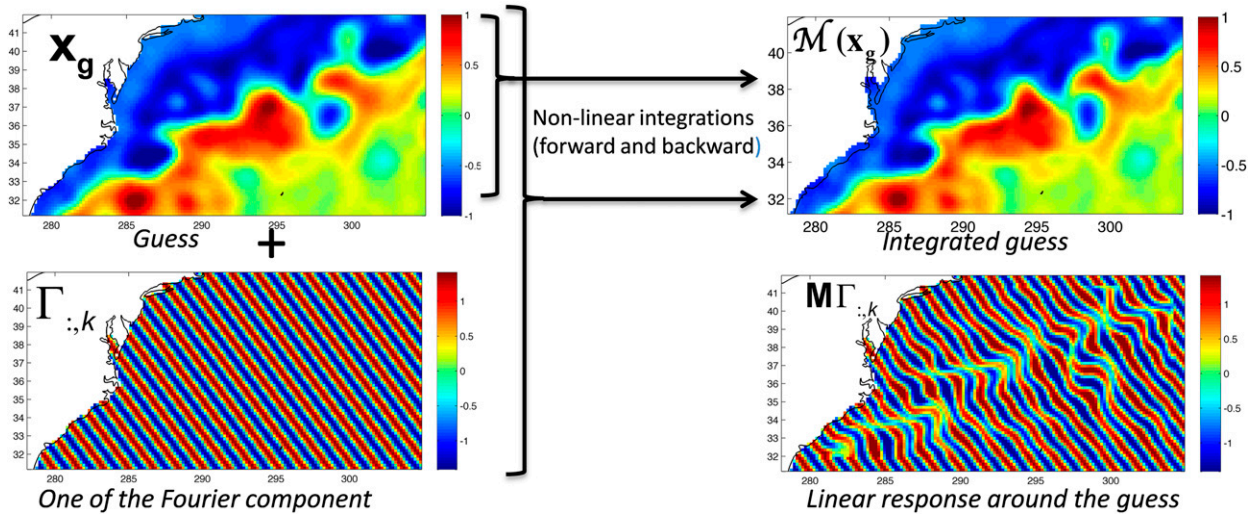


FIG. 2. Scheme of the Green's function computation. (upper left) The current guess field and (lower left) the normalized Fourier component. The propagator integration of the current guess and the current guess plus the Fourier component with infinitesimal amplitude is then performed. (upper right) The result of the guess integration is shown. (lower right) The difference between the two integrated fields, renormalized by the amplitude of the Fourier mode, is shown. This final field, collocated at observation points in time and space, constitutes the column of the  $\mathbf{G}$  matrix [Eq. (14)] for the corresponding Fourier component.

c. A look at the representer functions

The covariance between a particular grid point and the rest of the domain at different times is an interesting indicator of the mapping model characteristics. For the standard mapping, this correlation is directly given by the covariance model Eq. (2). For dynamic mapping, the covariance is  $\mathbf{G}_0 \mathbf{P} \mathbf{G}^T$ , where  $\mathbf{G}_0$  is the Green function matrix at the reference time (nonpropagated) and  $\mathbf{G}$  is the propagated Green function matrix up to a particular time. After normalization by the variance, the correlation fields have been represented in Fig. 3 for different times and for both the standard mapping model and dynamic mapping model. At time of analysis (central

panels) the correlations are identical; they both follow the spatial covariance model of Eq. (3), by definition. However, with time evolving, the correlation fields become very different and specific because of the propagator integration. Far in time (e.g., 10 days) higher values are encountered locally and with an offset from the reference point, indicating that some information can be extracted from observations farther in time in the dynamic mapping case.

d. Results and comparison with standard mapping

The analysis with standard and dynamic mapping has been performed on 1 years' worth of data. The results are presented and analyzed in this section, from both direct

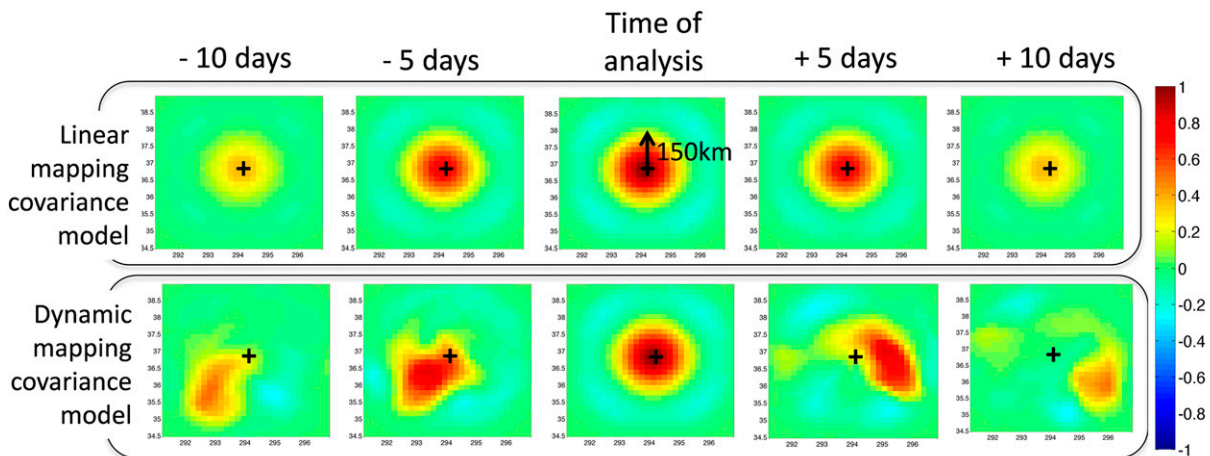


FIG. 3. Representers of the correlation fields between a given point at the time of analysis and the rest of the domain for different times ranging from  $-10$  to  $+10$  days. (top) The fields for the standard mapping and (bottom) the fields for the dynamic mapping.

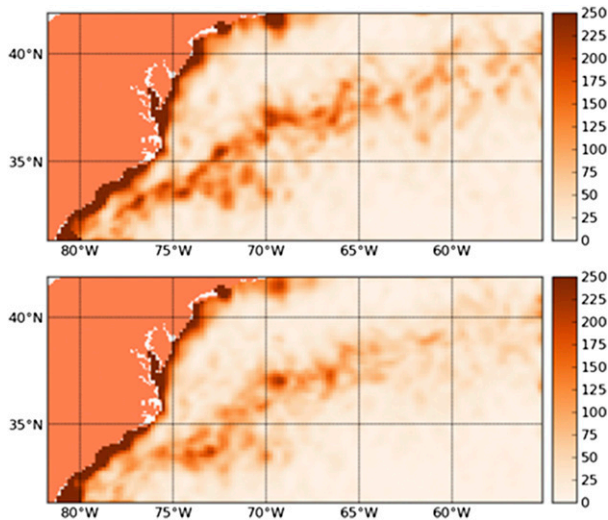


FIG. 4. (top) Variance of the difference between the linear solution and the reference run in SLA. (bottom) As in (top) but with the dynamic solution. Units:  $\text{cm}^2$ .

diagnostics (error maps) and spectral diagnostics (mean power spectral densities and spectral coherences).

Figure 4 shows the maps of error variance between the reference run and the two sets of reconstructions over 1 year. The improvements of the dynamic solution over the linear solution are clear in the Gulf Stream current where the errors are reduced by almost 30% on average. However, the improvements are not significant along the continental shelf where the errors remain strong. In this area, the barotropic mode (not considered in the dynamic propagator) may be important. Further dynamic considerations would be therefore worth investigating, in order to account for other modes or dynamics in such specific coastal regions. It is nevertheless encouraging that the dynamic solution with only the first baroclinic mode is not worse than the linear solution on the continental shelf.

Figure 5 is an illustration of the results for a particular time, showing in the left column the SSH and in the right column the corresponding geostrophic velocity. The top panels are the reference fields, which are instant snapshots of the truth at time of analysis. The second row is the interpolated fields with the linear solution. As expected, from the comparison with the truth, the large scales (largest  $\sim 500$ -km eddies) are well resolved but important errors remain at smaller scales due to the sparse observation sampling in time and space. For example, the  $\sim 125$ -km eddy at  $35^\circ\text{N}$ ,  $289^\circ\text{E}$  is not resolved. The third row is the interpolated fields with the dynamic solution, which is able to resolve smaller scales accurately. For example, the above-mentioned eddy is partially resolved. The error fields (the fourth and fifth rows) indicate significant

improvements consistent with the error variance diagnostics presented above, for both SSH and its derivative geostrophic velocity.

Some scale-dependent diagnostics have been performed on the whole series of analyses with respect to the reference in order to better quantify the improvements as a function of scale. Indeed, given the steep SLA spectral slope (between  $-3$  and  $-4$ ), the error variance diagnostic mentioned above principally reflects the larger scale errors. It is therefore interesting to look at spectral content, with a particular attention on the phases indicating whether a given scale is phased or not between the reference and the interpolation reconstructions. The upper panel of Fig. 6 shows the power spectral density of the reference (black), the linear interpolation reconstruction (blue) and the dynamic interpolation reconstruction (red). The spectrum of linear interpolation starts dropping below the reference spectrum at scales above  $\sim 300$  km, and has a steep drop below 140 km. However, the dynamic interpolation spectrum seems to better represent the energy below 300 km, and the firm drop only occurs at  $\sim 120$  km. However, it is important to note that correct energy does not mean absence of errors, so comparing the phases is relevant to assess if a given scale is well resolved or not. To do so, the cross-power spectral densities have been computed between the interpolated fields and the reference fields. After normalization with the square root of the power spectral density of each field, we obtain the so-called spectral coherence represented in the lower panel. This diagnostic clearly reveals that the interpolated fields are well phased (spectral coherence close to 1) from long wavelengths down to a range of scales where coherence progressively drops toward zero. Here, it is clear that the dynamic interpolation outperforms the linear interpolation. The wavelength of 0.5 coherence, which can be considered as a threshold for assessing resolving capabilities, is located at  $\sim 145$  km for linear interpolation and  $\sim 125$  km for dynamic interpolation. This highlights the better resolving capabilities of dynamic interpolation over linear interpolation. We found that unlike the power spectral density, the spectral coherence was insensitive to the covariance parameters. The systematic gain in the spectral coherence, especially for scales between 125 and 250 km, seems inherent to the dynamic propagation that allows for better resolution of the phase of small eddies. These spectral coherences can be compared with those obtained by Ubelmann et al. (2015) from an idealized framework where interpolation was performed between two full images of SSH. While being significant, the relative gain from linear to dynamic interpolation is less pronounced here. We have two explanations for

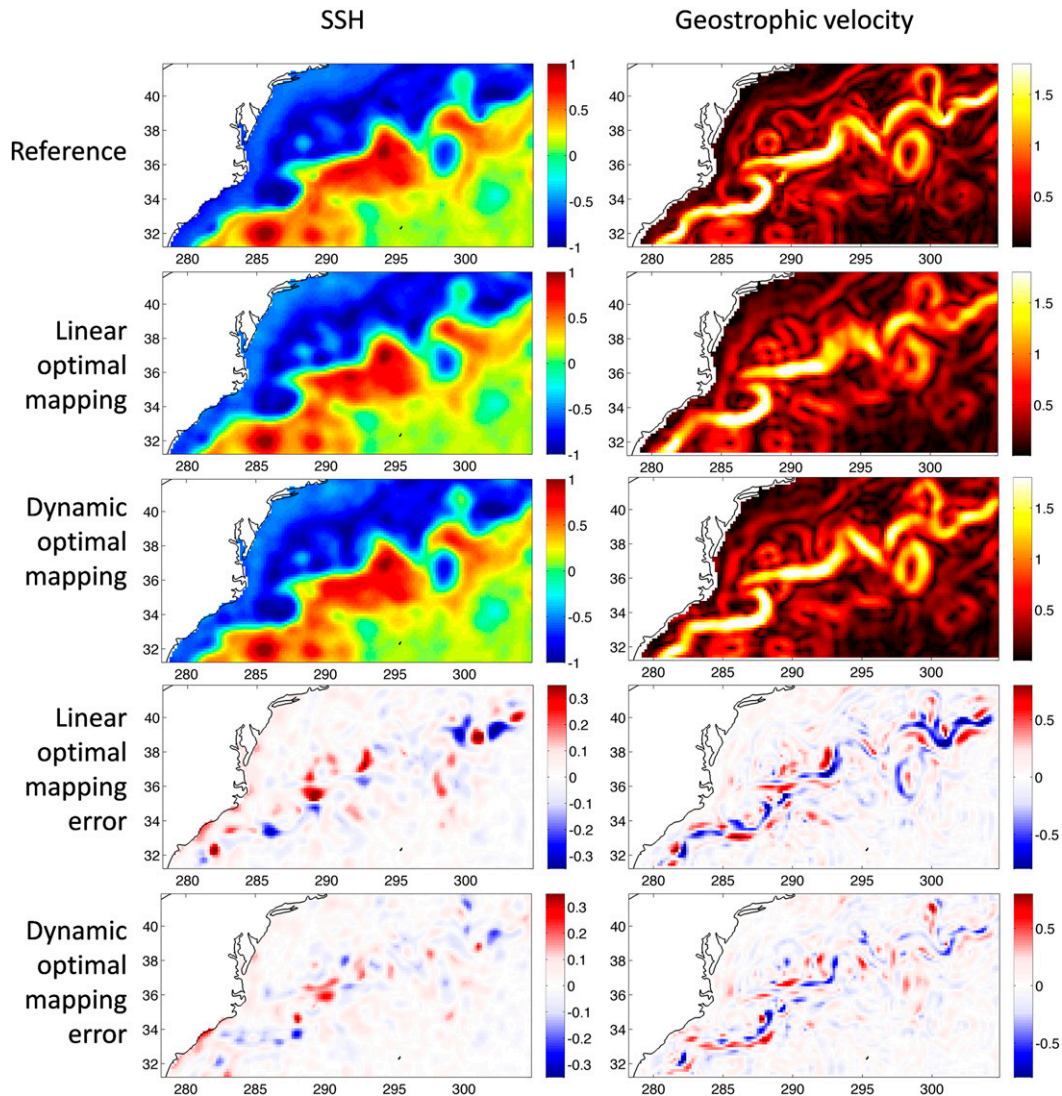


FIG. 5. Comparison of the results at one particular date, for both standard mapping and dynamic mapping. The fields and associated residual errors are shown for (left) the SSH and (right) its derivative the geostrophic velocity.

this. First, this more realistic case treats larger scales (because of the limited number of nadir satellites and the noise considered) and it was shown in [Ubelmann et al. \(2015\)](#) that the relative performances were decreasing as scales increase, because the nonlinearity is less important (larger scales are more linear). Second, these realistic data are distributed all over in time and space, whereas in the idealized case the observations were snapshots separated in time (with no observations in between). Since the introduction of dynamics allows reduction of the time decorrelation, its effect should be more pronounced when the observations suffer from time resolution like in the idealized case by construction. However, it is interesting to note that in this study simulating a realistic dataset of altimeter data, the

dynamic interpolation method is still of interest in the strong western boundary currents.

## 5. Conclusions

This study presented a practical implementation of the dynamic interpolation introduced in [Ubelmann et al. 2015](#). We followed here an inverse approach resolving a 3D (space + time) least squares problem similar to the standard optimal interpolation. However, unlike standard inversions following linear models, we proposed to use a locally linearized propagator with appropriate correction term for nonlinear evolutions of the local state in the innovations. Significant improvements from linear optimal mapping to nonlinear dynamic mapping

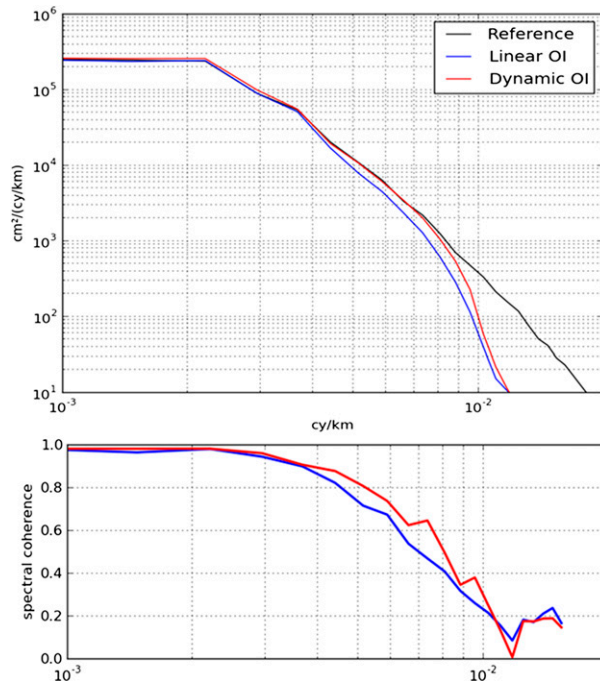


FIG. 6. (top) 1-yr averaged power spectral densities computed in a box ranging from longitudes 288°–305° and latitudes 32°–40°. In black is the reference run considered as the unknown truth. In blue is the solution for linear interpolation and in red for dynamic interpolation. (bottom) 1-yr averaged spectral coherences over the same box, between linear interpolation and reference (blue) and dynamic interpolation and reference (red).

have been shown, which encourages applying the method to process new maps of real altimetry data.

This method can be applied to any nonlinear propagator. Although this simple quasigeostrophic (QG) propagator performs efficiently in the Gulf Stream region, more sophisticated propagators may have to be developed for other regions. For instance, in coastal regions we may implement topography effects, for example, through adjustment of the Rossby radius and the addition of a barotropic mode if this latter is dominant. Also, in the equatorial regions, the quasigeostrophic (QG) propagator would clearly not be an appropriate choice. Other propagators (maybe simply linear waveguides) may be developed for these regions.

This dynamic interpolation method presents some specific features with respect to data assimilation in OGCMs. Unlike OGCM data assimilation, the solution is not a model trajectory (or a sequentially adjusted model trajectory). Here, the propagator is only used to determine a better covariance, but the analysis is performed separately from the mean sea surface height (MSSH) background, not from a model trajectory. For example, in the absence of observations, our mapping solution is the MSSH, not a free model run. The term “propagator” is meant to distinguish from an OGCM: the

propagator only represents a deterministic SSH evolution, not necessarily a realistic evolution with input of energy, eddy generation, and other physics. In this sense, the dynamic interpolation keeps strong fidelity with the data. Beyond the deterministic evolution accounted for, all other dynamics are parameterized in a specific covariance matrix, like all dynamics are in standard interpolation.

*Acknowledgments.* Part of the research presented in the paper was carried out at the Jet Propulsion Laboratory, California Institute of Technology, under contract with the National Aeronautics and Space Administration. Support from the SWOT project is acknowledged.

## REFERENCES

- Arhan, M., and A. Colin de Verdière, 1985: Dynamics of eddy motions in the eastern North Atlantic. *J. Phys. Oceanogr.*, **15**, 153–170, doi:10.1175/1520-0485(1985)015<0153:DOEMIT>2.0.CO;2.
- AVISO, 2015: SSALTO/DUACS user handbook: (M)SLA and (M)ADT near-real time and delayed time products. Issue 4.4, CNES CLS-DOS-NT-06-034, SALP-MU-P-EA-21065-CLS, 66 pp. [Available online at [http://www.aviso.oceanobs.com/fileadmin/documents/data/tools/hdbk\\_duacs.pdf](http://www.aviso.oceanobs.com/fileadmin/documents/data/tools/hdbk_duacs.pdf).]
- Bretherton, F. P., R. E. Davis, and C. B. Fandry, 1976: A technique for objective analysis and design of oceanographic experiment applied to MODE-73. *Deep-Sea Res. Oceanogr. Abstr.*, **23**, 559–582, doi:10.1016/0011-7471(76)90001-2.
- Ducet, N., P.-Y. Le Traon, and G. Reverdin, 2000: Global high-resolution mapping of ocean circulation from TOPEX/Poseidon and ERS-1 and -2. *J. Geophys. Res.*, **105**, 19 477–19 498, doi:10.1029/2000JC900063.
- Hill, C., D. Menemenlis, B. Ciotti, and C. Henze, 2007: Investigating solution convergence in a global ocean model using a 2048-processor cluster of distributed shared memory machines. *Sci. Program.*, **15**, 107–115, doi:10.1155/2007/458463.
- Le Traon, P.-Y., F. Nadal, and N. Ducet, 1998: An improved mapping method of multisatellite altimeter data. *J. Atmos. Oceanic Technol.*, **15**, 522–534, doi:10.1175/1520-0426(1998)015<0522:AIMMOM>2.0.CO;2.
- Menemenlis, D., I. Fukumori, and T. Lee, 2005: Using Green’s functions to calibrate an ocean general circulation model. *Mon. Wea. Rev.*, **133**, 1224–1240, doi:10.1175/MWR2912.1.
- , J. Campin, P. Heimbach, C. Hill, T. Lee, A. Nguyen, M. Schodlok, and H. Zhang, 2008: ECCO2: High resolution global ocean and sea ice data synthesis. *Mercator Ocean Quarterly Newsletter*, No. 31, Mercator Ocean, Ramonville Saint-Agne, France, 13–21.
- Ubelmann, C., P. Klein, and L.-L. Fu, 2015: Dynamic interpolation of sea surface height and potential applications for future high-resolution altimetry mapping. *J. Atmos. Oceanic Technol.*, **32**, 177–184, doi:10.1175/JTECH-D-14-00152.1.
- Wunsch, C., 1996: *The Ocean Circulation Inverse Problem*. Cambridge University Press, 442 pp.
- , 1997: The vertical partition of oceanic horizontal kinetic energy. *J. Phys. Oceanogr.*, **27**, 1770–1794, doi:10.1175/1520-0485(1997)027<1770:TVPOOH>2.0.CO;2.
- Xu, Y., and L.-L. Fu, 2011: Global variability of the wavenumber spectrum of oceanic mesoscale turbulence. *J. Phys. Oceanogr.*, **41**, 802–809, doi:10.1175/2010JPO4558.1.